catalysts

MDPI

Article

Ni_5P_4-NiP_2-Ni_2P Nanocomposites Tangled with N-Doped Carbon for Enhanced Electrochemical Hydrogen Evolution in Acidic and Alkaline Solutions

Miaomiao Pei [1], Xiaowei Song [1,2,*], Haihong Zhong [2,3,*], Luis Alberto Estudillo-Wong [4], Yingchun Gao [1], Tongmengyao Jin [1], Ju Huang [1], Yali Wang [1], Jun Yang [5] and Yongjun Feng [2,*]

1 Key Laboratory of Functional Coordination Compounds of Anhui Higher Education Institutes, School of Chemistry and Chemical Engineering, Anqing Normal University, Anqing 246011, China
2 State Key Laboratory of Chemical Resource Engineering, Beijing Engineering Center for Hierarchical Catalysts, College of Chemistry, Beijing University of Chemical Technology, No. 15 Beisanhuan East Road, Beijing 100029, China
3 College of Science, Hainan University, Haikou 570228, China
4 Departamento de Biociencias e Ingeniería, CIIEMAD-IPN, Instituto Politécnico Nacional, Calle 30 de Junio de 1520, Alcaldía GAM, Ciudad de México 07340, Mexico
5 State Key Laboratory of Multiphase Complex Systems, Institute of Process Engineering, Chinese Academy of Sciences, Beijing 100190, China
* Correspondence: songxw@aqnu.edu.cn (X.S.); hzhong@buct.edu.cn (H.Z.); yjfeng@mail.buct.edu.cn (Y.F.)

check for updates

Citation: Pei, M.; Song, X.; Zhong, H.; Estudillo-Wong, L.A.; Gao, Y.; Jin, T.; Huang, J.; Wang, Y.; Yang, J.; Feng, Y. Ni_5P_4-NiP_2-Ni_2P Nanocomposites Tangled with N-Doped Carbon for Enhanced Electrochemical Hydrogen Evolution in Acidic and Alkaline Solutions. *Catalysts* **2022**, *12*, 1650. https://doi.org/10.3390/catal12121650

Academic Editors: Guillermo Ahumada and Jonathan Cisterna

Received: 21 November 2022
Accepted: 13 December 2022
Published: 15 December 2022

Abstract: Heterostructured non-precious metal phosphides have attracted increasing attention in the development of high-performance catalysts for hydrogen evolution reaction (HER), particularly in acidic media. Herein, a catalyst composed of ternary Ni_5P_4-NiP_2-Ni_2P nanocomposites and N-doped carbon nanotubes/carbon particulates (Ni_5P_4-NiP_2-Ni_2P/NC) was prepared from a Ni-containing hybrid precursor through approaches of a successive carbonization and phosphating reaction. Benefiting from the synergistic effect from three-component nickel phosphides and the support role of porous carbon network, the Ni_5P_4-NiP_2-Ni_2P/N-doped carbon catalyst presents the promising HER performance with overpotentials of 168 and 202 mV at the current density of 10 mA cm^{-2} and Tafel slopes of 69.0 and 74 mV dec^{-1} in both acidic and alkaline solutions, respectively, which surpasses the Ni_2P/N-doped carbon counterpart. This work provides an effective strategy for the preparation and development of highly efficient HER non-precious metal electrocatalysts by creating heterostructure in acidic and alkaline media.

Keywords: three-component nickel phosphides; N-doped carbon nanotubes; hydrogen evolution reaction; mesoporous carbon network; synergistic effect

1. Introduction

Hydrogen is regarded as one of the most fascinating fuel carriers, with the ability to tackle the ever-growing energy demand and lessen the emissions of greenhouse gases [1,2]. Among those reported techniques, water electrolysis is one of the effective and sustainable approaches to produce high-purity hydrogen, which depends mainly on high-performance electrocatalysts for the cathodic hydrogen evolution reaction (HER) [3]. To date, Pt-based materials remain the state-of-the-art catalysts for the HER but suffer from high cost, low abundance, and difficult commercial applications. In order to supersede the Pt-based catalysts, it is desirable to explore non-precious metal electrocatalysts [4].

Recently, nickel (Ni) as the center element of [NiFe]-hydrogenases has gained increasing attention in developing Ni-based HER catalysts, including Ni-based sulfides, nitrides, selenides, and phosphides [4–12]. Among them, dinickel phosphide (Ni_2P) has been widely investigated for HER, owing to its high performance and low cost [3,11,13–18]. Yet, improving the electrocatalytic performance of Ni_2P for practical application is still desired [19–24].

Thus, in recent years, development of heterostructured nickel phosphides is considered to be a promising way to enhance HER intrinsic activity because of the potential synergistic effect among different components. For instance, biphasic nickel phosphides, such as Ni_2P/NiP_2 [25], Ni_2P/Ni_5P_4 [26–28], and Ni_2P-$Ni_{12}P_5$ [29,30], have emerged as superior HER electrocatalysts. Yet, the design of nickel phosphide catalysts with high conductivity and stability is still challenging.

One effective strategy is to grow nickel phosphide species on conductive substrates (e.g., nickel foam, carbon cloth, carbon sheets, graphene, and carbon nanotubes), inhibiting the agglomeration of catalysts and, thus, further enhancing catalytic activity and stability [31–34]. Among them, three-dimensional (3D) porous carbon materials favor the exposure of the active sites [35,36]. For instance, Mao and co-workers [37] employed the graphene as the supporting network to support the chainmail Ni_2P nanoparticles encapsulated by ultrathin P-doped carbon shell for efficient hydrogen generation. Chen and co-workers [38] introduced reduced graphene oxide to fabricate carbon nanotubes/graphene-confined Ni-$Ni_{12}P_5$ nanoparticles towards sustainable hydrogen evolution. Lan and co-workers [39] reported commercial multi-walled carbon nanotubes supporting polynary nickel phosphide nanoflowers for HER with enhanced performance. Therefore, it might also be a good route to support nickel phosphides using in situ-formed carbon materials.

Herein, combining the synergy effect of multicomponents and the strategies of in situ-forming carbon substrates, a catalyst composed of ternary Ni_5P_4-NiP_2-Ni_2P nanocomposites supported on the N-doped carbon nanotubes/carbon particulates (Ni_5P_4-NiP_2-Ni_2P/NC) was prepared from a hybrid precursor $Ni(bpy)(NO_3)_2$/g-C_3N_4/$Ni(dmgH)_2$ through carbonization and subsequent phosphating reaction. It is worth mentioning that the phosphating reaction proceeds via a sodium borohydride ($NaBH_4$)-assisted sodium hypophosphite (NaH_2PO_2) method. The in situ-grown N-doped carbon nanotubes tangled with N-doped carbon particulates ensure the intimate contact with nickel phosphides and provide the interconnected 3D mesoporous structure, certainly improving the accessibility of active sites. The obtained Ni_5P_4-NiP_2-Ni_2P/N-doped carbon catalyst (Ni_5P_4-NiP_2-Ni_2P/NC) revealed good HER activity in both 0.5 M H_2SO_4 and 1 M KOH solutions, outperforming the Ni_2P/N-doped carbon counterpart (Ni_2P/NC) under the same conditions. Furthermore, the former catalyst maintained favorable stability in acid medium.

2. Results and Discussion

2.1. Characterizations of Morphology and Structure

Figure 1 illustrates that the synthetic process of the Ni_5P_4-NiP_2-Ni_2P/NC. Both 4,4′-bipyridine (bpy) and dimethylglyoxime ($dmgH_2$) has strong coordination with Ni^{2+} to generate coordinate materials, which can be employed as precursors to prepare nitrogen-doped carbon materials via pyrolysis. In addition, g-C_3N_4 is a widely used self-sacrifice template in the preparation of porous materials [40]. Therefore, we prepared a hybrid precursor coupling g-C_3N_4 and nickel coordination materials through two-step coordination reactions. First, a simple solvothermal reaction led to the formation of $Ni(bpy)(NO_3)_2$/g-C_3N_4 hybrids, which were further etched by $dmgH_2$ to form $Ni(dmgH)_2$ microwires, ensuring the high dispersion of nickel source in the precursor matrix. Figure S1 presents the XRD pattern of $Ni(bpy)(NO_3)_2$/g-C_3N_4/$Ni(dmgH)_2$ and the single crystal structure of $Ni(bpy)(NO_3)_2$. One can observe a broad peak at ~27.3°/2θ assigned to the (002) plane of the g-C_3N_4 phase [41]. The simulated XRD peaks from single crystal data of $Ni(bpy)(NO_3)_2$ and $Ni(dmgH)_2$ match well with the powder XRD results, indicating the successful formation of $Ni(bpy)(NO_3)_2$/g-C_3N_4/$Ni(dmgH)_2$. As displayed in Figure 2a, the needle-like $Ni(dmgH)_2$ grows from the surface of bulk $Ni(bpy)(NO_3)_2$ and extends into the g-C_3N_4 matrix [42]. After pyrolysis, the precursor was carbonized into N-doped carbon-network-twined Ni nanoparticles (Ni/NC), and nickel sources were converted into metallic Ni nanoparticles, which were distributed in the in situ-generated N-doped carbon networks and subsequently transformed into nickel phosphide nanocomposites via the $NaBH_4$ assisted phosphorization.

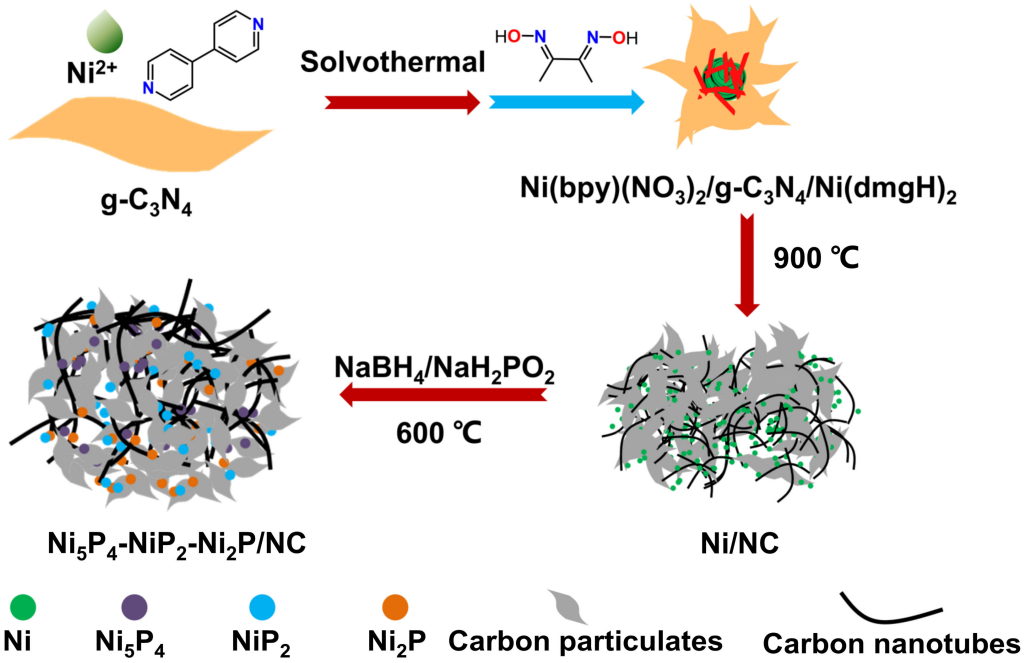

Figure 1. Illustration drawing of the synthesis process of Ni_5P_4-NiP_2-Ni_2P/NC.

The SEM image of Ni/NC shows that carbon nanotubes and amorphous carbon particulates are intertwined into a 3D network structure, cf. Figure 2b. When the calcination temperature exceeds 700 °C, g-C_3N_4 is decomposed into carbon nitride fragments, such as $C_2N_2^+$, $C_3N_2^+$, and $C_3N_3^+$, which can be further carbonized into N-doped carbon nanotubes under the catalysis of in situ-formed nickel nanoparticles [43]. Some bright points emerge on the surface of Ni/NC, which could be metallic nickel particles. Compared with Ni/NC, Ni_2P/NC exhibits similar heterogeneous morphologies with slightly larger nanosheets, cf. Figure 2c. In addition, no obvious Ni particles can be observed on the surface of Ni_2P/NC. After $NaBH_4$-assisted phosphorization of Ni/NC, seen in Figure 2d, amorphous carbon structures are fused into flocculent-like carbon particulates, which aggregate on the surface of carbon nanotube skeletons to form a 3D network.

Figure 2e further shows the XRD patterns of three samples. One observes that Ni/NC presents three peaks located at 44.5°, 51.8°, and 76.4°/2θ, corresponding to the (111), (200), and (220) crystal planes of cubic Ni (PDF#87-0712). Additionally, the peak located at 25.9° can be assigned to the (002) facet of graphitic carbon [44]. For the sample Ni_5P_4-NiP_2-Ni_2P/NC, three diffraction peaks at 52.9°, 45.2°, and 36.1°/2θ are assigned to (303), (204) and (104) crystal planes of Ni_5P_4 (PDF#65-2075, hexagonal crystal system), respectively. The diffraction peaks at 55.8°, 36.8°, 32.7°, and 28.2°/2θ are individually assigned to (311), (210), (200), and (111) crystal planes of NiP_2 phase (PDF#73-0436, cubic crystal system). Three additional diffraction peaks at 54.1°, 44.6°, and 40.5°/2θ are assigned to (300), (021), and (111) crystal planes of Ni_2P (PDF#65-3544, hexagonal crystal system), respectively. These results indicate that Ni_5P_4-NiP_2-Ni_2P/NC is composed of Ni_5P_4, Ni_2P, and NiP_2 phases as well as graphitic carbon. In comparison, when the $NaBH_4$ is absent during the phosphating reaction, the XRD peaks for Ni_2P/NC could all be indexed to Ni_2P (PDF#65-3544, cubic crystal system). To determine the mass percentage of nickel phosphide polymorphs in the sample Ni_5P_4-NiP_2-Ni_2P/NC, the Rietveld Refinement Method (RRM) was carried out using Crystallographic Open Database (COD) for Ni_5P_4 (COD#221-4342), Ni_2P (COD#152-2619), and NiP_2 (COD#901-2503) phases. Figure 2f and Table S1 further display the microstructural properties obtained by RRM analysis. Here, Ni_5P_4 ($P6_3mc$) and NiP_2 (Pa-3) are the main phases in the sample, with crystallite average size of 90.4 ± 3.4 and 70.6 ± 1.3 nm, respectively. In addition, the Ni_2P (P-62m) phase provides the lowest composition with a crystallite average size of 30.3 ± 1.3 nm.

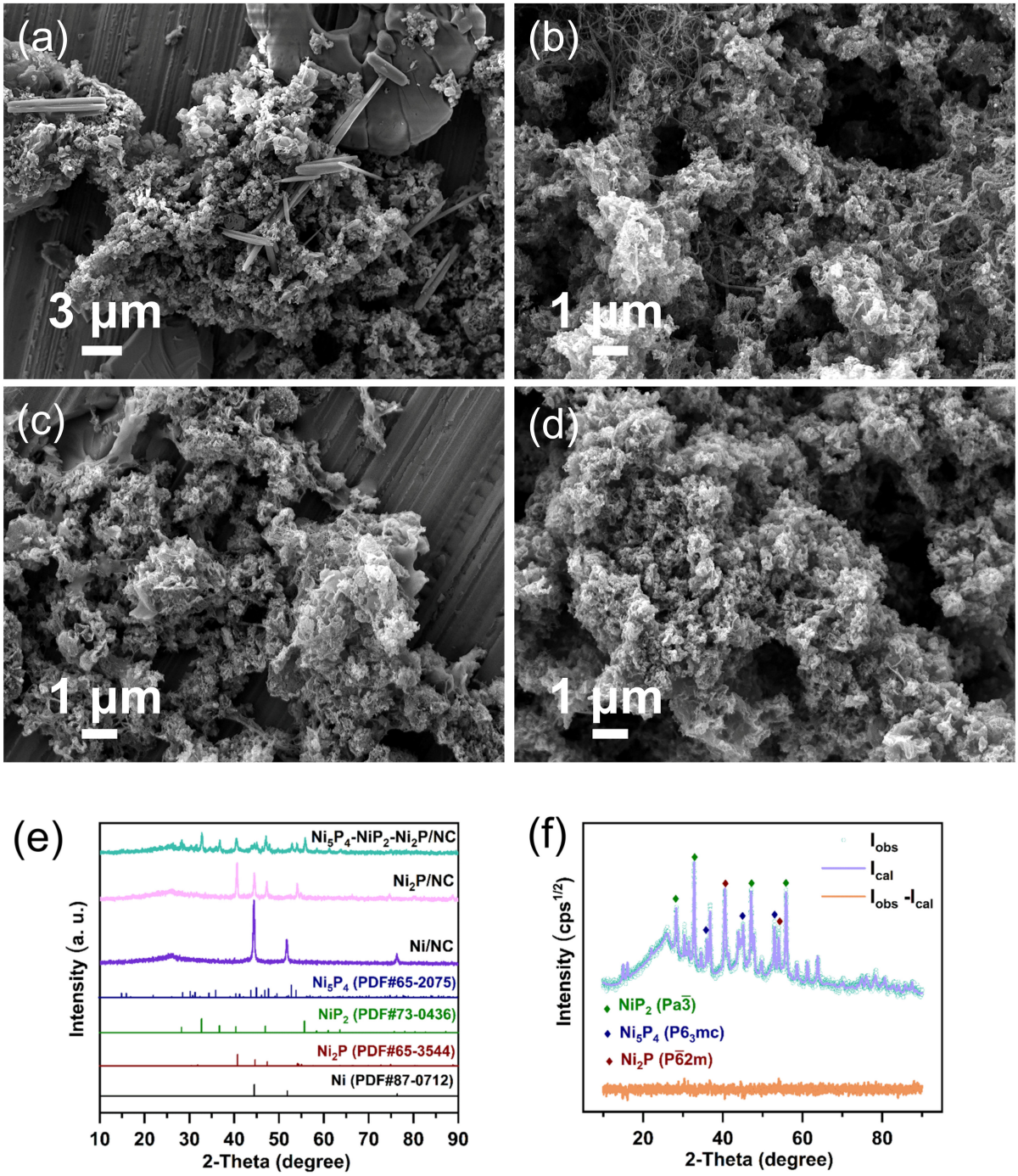

Figure 2. SEM images of (**a**) $Ni(bpy)(NO_3)_2/g\text{-}C_3N_4/Ni(dmgH)_2$, (**b**) Ni/NC, (**c**) Ni_2P/NC, and (**d**) Ni_5P_4-NiP_2-Ni_2P/NC; (**e**) XRD patterns of Ni/NC, Ni_2P/NC, and Ni_5P_4-NiP_2-Ni_2P/NC samples; (**f**) XRD experimental and fitting patterns for Ni_5P_4-NiP_2-Ni_2P/NC. G-of-F (R_{wp}%) parameter is 1.12 (4.1).

Figure 3a–c demonstrate TEM images of Ni_5P_4-NiP_2-Ni_2P/NC. Here, nickel phosphide nanoparticles with sizes in the range of 10 to 100 nm are distributed in the carbon matrix composed of carbon nanotubes and carbon particulates. Furthermore, the SAED pattern in Figure 3d shows the polycrystalline diffraction rings and scattering dots, indicating the coexistence of Ni_5P_4, Ni_2P, and NiP_2. HRTEM analysis reveals that the lattice spacing of 0.32 nm is ascribed to the (111) plane of NiP_2 phase, cf. Figure 3e, and the lattice spacings of 0.55 and 0.22 nm belong to the (002) plane of Ni_5P_4 and the (111) plane of Ni_2P in Figure 3f,

respectively. The Ni_5P_4 nanoparticles are wrapped by few-layer carbon shells with a lattice spacing of 0.34 nm, corresponding to the (002) plane of graphitic carbon. The elemental mapping images confirm that these nickel phosphide polymorphs appear as irregularly shaped particles in the nitrogen-doped carbon matrix, cf. Figure 3g. Combined with the XRD patterns, these TEM results clearly indicate that the sample Ni_5P_4-NiP_2-Ni_2P/NC consists of unique triphasic Ni_5P_4-NiP_2-Ni_2P nanocomposites.

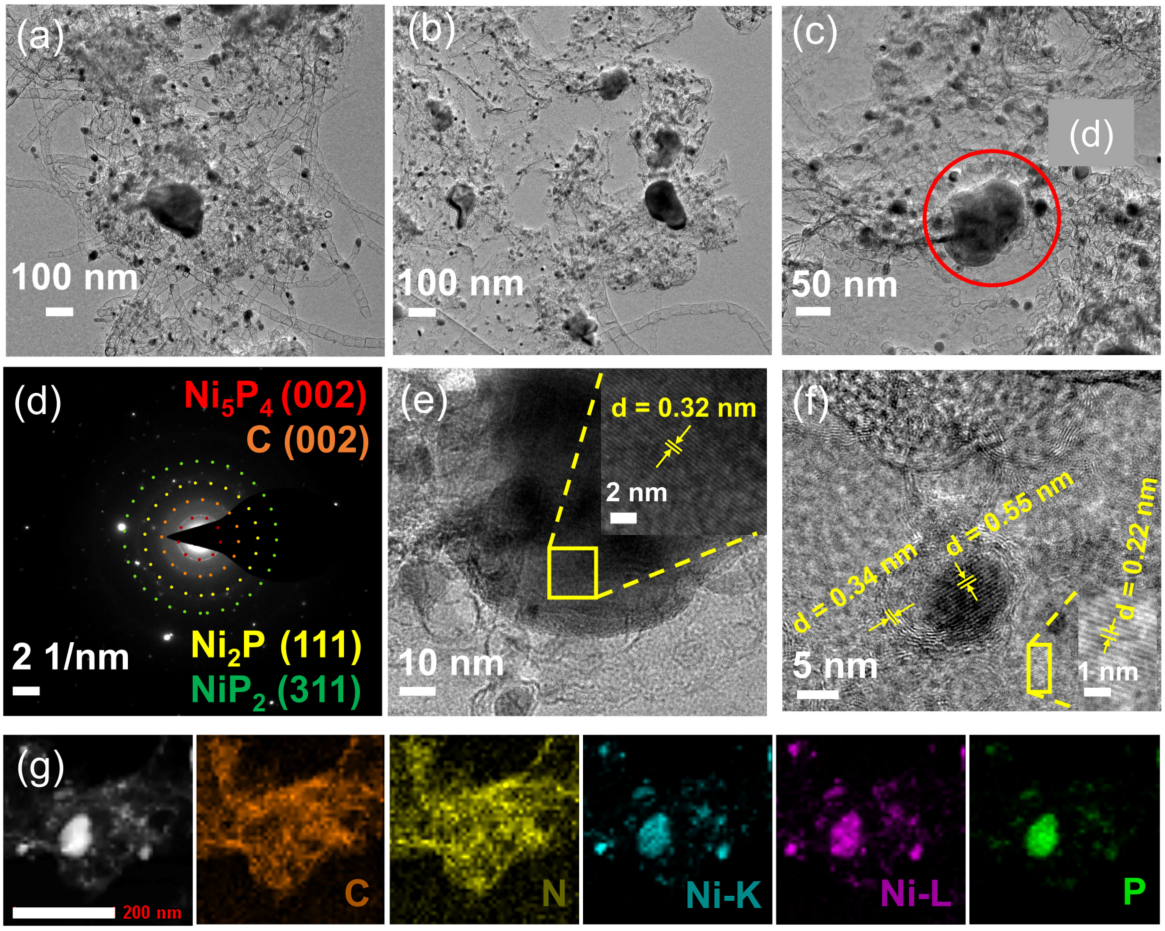

Figure 3. (**a**–**c**) TEM, (**d**) SAED pattern, (**e**,**f**) HRTEM, and (**g**) the corresponding elemental (C, N, Ni, and P) mappings of Ni_5P_4-NiP_2-Ni_2P/NC.

The N_2 adsorption–desorption isotherms of three samples in Figure 4a exhibit type IV with an H2-type hysteresis loop in the medium pressure region. The hysteresis feature suggests the capillary condensation in the interconnected mesoporous [45]. Figure 4b further shows the mesoporous size distribution in the range from 4 nm to 33 nm. The Brunauer–Emmett–Teller (BET) surface areas are individually calculated as 295.4, 110.3, and 207.6 m^2 g^{-1} for Ni/NC, Ni_2P/NC, and Ni_5P_4-NiP_2-Ni_2P/NC, respectively. The BET surface area difference among Ni/NC, Ni_2P/NC, and Ni_5P_4-NiP_2-Ni_2P/NC could correlate with multiple factors, including the size effect, the structural features of carbon network, and the composition of nickel phosphides [46–48]. The mesoporous structure and large specific surface area for Ni_5P_4-NiP_2-Ni_2P/NC aid the contact between the active sites and the electrolyte and then improve the electrocatalytic activity [40].

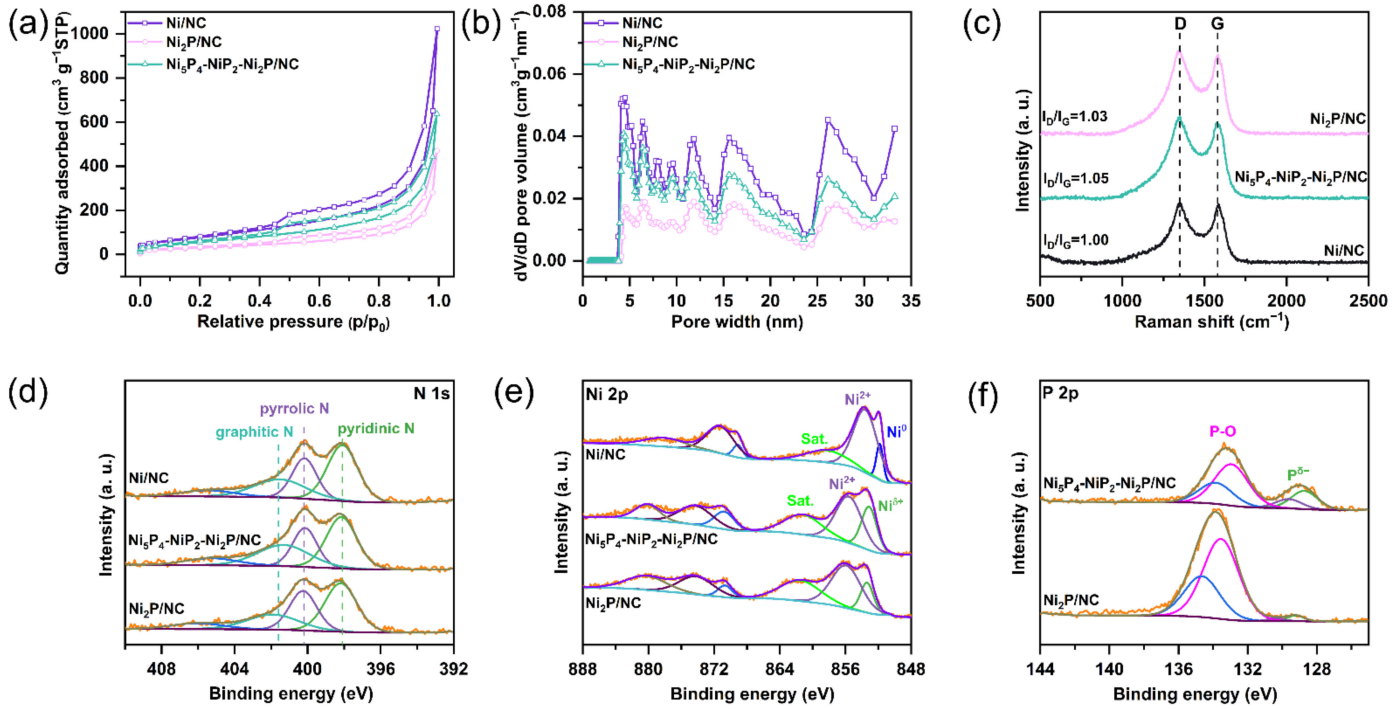

Figure 4. (**a**) N_2 adsorption–desorption isotherms and (**b**) pore-size distribution of the samples Ni/NC, Ni_2P/NC, and Ni_5P_4-NiP_2-Ni_2P/NC; (**c**) Raman spectra of Ni/NC, Ni_2P/NC, and Ni_5P_4-NiP_2-Ni_2P/NC; High-resolution XPS spectra of (**d**) N 1s, (**e**) Ni 2p, and (**f**) P 2p for all samples.

Figure 4c displays Raman spectra of three samples with two typical bands centered at approximately 1350 and 1580 cm^{-1}, which correspond to the structural defect carbon (D band) and graphitization carbon (G band), respectively. The intensity ratio of D and G-band (I_D/I_G) is approximately 1.00, 1.03, and 1.05 for Ni/NC, Ni_2P/NC, and Ni_5P_4-NiP_2-Ni_2P/NC, respectively, suggesting that the phosphorization results in more defect carbon structures.

Figure S2 demonstrates the XPS survey spectra for all the samples, and Table S2 lists the relative atomic percentages of elements. The high-resolution C 1s spectra (Figure S3) for each sample show four fitted peaks centered at 283.9, 284.6, 287.6, and 290.9 eV, which are assigned to C-C/C=C, C-N/C-O, O=C, and O-C=O bonds, respectively [43]. Figure 4d presents the high-resolution N 1s spectra for all samples. The nitrogen chemical states correspond to four types of N configuration, including pyridinic N (398.2 eV), pyrrolic N (400.2 eV), graphitic N (401.3 eV), and oxidized N (405.3 eV) [49]. Furthermore, Figure 4e shows the comparative high-resolution Ni 2p spectra of three samples. The peak at 851.8 eV appears in Ni/NC, confirming the presence of zero-valent Ni. The sample Ni_5P_4-NiP_2-Ni_2P/NC exhibits two peaks located at 853.1 and 870.8 eV, which correspond to Ni $2p_{3/2}$ and Ni $2p_{1/2}$ spin-orbits of $Ni^{\delta+}$ ($0 < \delta < 2$) in nickel phosphides, respectively. The peaks at 855.6 and 874.2 eV are attributed to Ni^{2+} in nickel phosphides and surface oxidized Ni species, while the peaks at 861.2 and 880.1 eV are assigned to satellite peaks [18]. Moreover, the deconvolution peaks of the Ni 2p band for Ni_2P/NC show a relatively low percentage of $Ni^{\delta+}$ related to those of Ni_5P_4-NiP_2-Ni_2P/NC (35% in Ni_5P_4-NiP_2-Ni_2P/NC vs. 22.8% in Ni_2P/NC). The peaks positioned at 128.7 and 129.6 eV in the high-resolution P 2p spectrum of Ni_5P_4-NiP_2-Ni_2P/NC are indexed to the P $2p_{3/2}$ and P $2p_{1/2}$ signals of the negatively charged $P^{\delta-}$ ($0 < \delta < 2$), respectively, Figure 4f. It is noteworthy that the $P^{\delta-}$ peaks of the Ni_2P/NC sample shifted to high binding energies, likely due to enhanced electron transfer from $P^{\delta-}$ to metal in metal-rich phosphides (Ni_2P) [50]. In addition, for Ni_5P_4-NiP_2-Ni_2P/NC and Ni_2P/NC, the main deconvolution peak at 132.9 eV is ascribed to the P-O species due to the surface oxidation of nickel phosphides [33,51]. In order to discover whether element B is doped into the carbon layer, the XPS high-resolution spectrum of

Ni_5P_4-NiP_2-Ni_2P/NC was recorded in the binding energy range of 180–200 eV. It must be pointed out that the peaks of B 1s and P 2s overlap in this region. The P 2s peak for Ni_5P_4-NiP_2-Ni_2P/NC is obtained from P 2p and subtracted from the overlapping area, while the residual peak intensity is almost zero, cf. Figures S4 and S5. Additionally, both Ni/NC and Ni_5P_4-NiP_2-Ni_2P/NC have almost similar carbon and nitrogen states, as observed from their high-resolution C 1s and N 1s spectra. This result indicates that the element B is not doped into the carbon layer. Furthermore, no obvious B 1s-XPS signal is observed in Ni/NC-B, as shown in Figure S6. Therefore, the $NaBH_4$ does not serve as a B-doping reagent in this system but does play a key role in producing polymorph nickel phosphide. In the phosphating process, the additional $NaBH_4$ could act as an oxidant agent to promote the formation of zero-valent P, resulting in the formation of P-rich nickel phosphide.

2.2. Electrochemical Performance in Acidic Solution

For non-precious metal electrocatalysts, it is a great challenge to use them in the acidic electrolyte. Here, the HER performance of the Ni_5P_4-NiP_2-Ni_2P/NC catalyst was first evaluated in a 0.5 M H_2SO_4 solution. For comparison, Ni_2P/NC, Ni/NC, and commercial Pt/C catalyst were also examined. In Figure 5a, the Pt/C electrode exhibits the best HER activity, with an overpotential of 40 mV at the current density of 10 mA cm^{-2} (referred to η_{10}), while the Ni_5P_4-NiP_2-Ni_2P/NC electrode shows the overpotential (η_{10}) of 168 mV, which is significantly better than Ni_2P/NC (247 mV) and Ni/NC (312 mV). In Figure 5b, the Tafel slope of the Pt/C is as low as 30 mV dec^{-1}, which agrees closely with the previous reports [26,35]. The Ni_5P_4-NiP_2-Ni_2P/NC exhibits a Tafel slope of 69 mV dec^{-1}, smaller than that of Ni_2P/NC (81 mV dec^{-1}) and Ni/NC (103 mV dec^{-1}) but larger than that of Pt/C. The Tafel slope of Ni_5P_4-NiP_2-Ni_2P/NC falls within the range of 40–120 mV dec^{-1}, implying that the electrochemical desorption is the rate-limiting step, and the Volmer–Heyrovsky route is responsible for this HER [33]. The electrocatalytic HER performance of Ni_5P_4-NiP_2-Ni_2P/NC is still inferior in relation to the Pt/C catalyst but approaches to, and even outperforms, that of nickel phosphide/carbon systems in the literature, such as Ni_2P/C [15], Ni_2P/CNS [52], Ni_2P@C-400 [53], Ni_2P-MOF [54], and Ni-$Ni_{12}P_5$@CNTs/rGO-0.5 [38], in acidic electrolytes, cf. Table S3. In Figure 5c, the Nyquist plots of these catalysts at the overpotential of 170 mV are fitted by a facile equivalent circuit, in which the charge-transfer resistance R_{ct} represents the HER kinetics, and a smaller R_{ct} value corresponds to the faster HER rate. The R_{ct} of Ni_5P_4-NiP_2-Ni_2P/NC (21.9 Ω) is lower than that of Ni_2P/NC (131.1 Ω), suggesting a much faster electron transfer from active sites of Ni_5P_4-NiP_2-Ni_2P/NC to protons during HER. Of note, the catalyst Ni/NC shows R_{ct} as high as 586.8 Ω, which may be due to the blockage of electron transfer at the electrode/solution interface caused by the corrosion of surface nickel particles in the acidic solution. These results further indicate that the HER activity of Ni_5P_4-NiP_2-Ni_2P/NC arises from nickel phosphide species.

In addition to electrocatalytic activity, the electrocatalytic stability is another key parameter, particularly for non-precious metal electrocatalysts in acidic electrolyte. Figure 5d shows chronopotentiometric results of Ni_5P_4-NiP_2-Ni_2P/NC at the current density of 10 mA·cm^{-2} in 0.5 M H_2SO_4. Here, after 20 h constant current electrolysis, the overpotential increases only 12 mV. Furthermore, from the insert graph, after 3000 cycles of CV scans at a scan rate of 100 mV s^{-1}, the overpotential of Ni_5P_4-NiP_2-Ni_2P/NC at the current density of 10 mA·cm^{-2} displays a slight shift of 3 mV, suggesting good stability in the long-term electrocatalytic process. Additionally, the SEM image after chronopotentiometric testing further confirms that the morphology of the Ni_5P_4-NiP_2-Ni_2P/NC maintains the original features (Figure S7). In addition, the structural stability of Ni_5P_4-NiP_2-Ni_2P/NC is revealed by its XPS spectra. The high-resolution XPS spectra of Ni 2p (Figure S8) and P 2p (Figure S9) display deconvoluted peaks like those of the fresh sample, validating the preferable electrocatalytic stability of Ni_5P_4-NiP_2-Ni_2P/NC in acidic solutions.

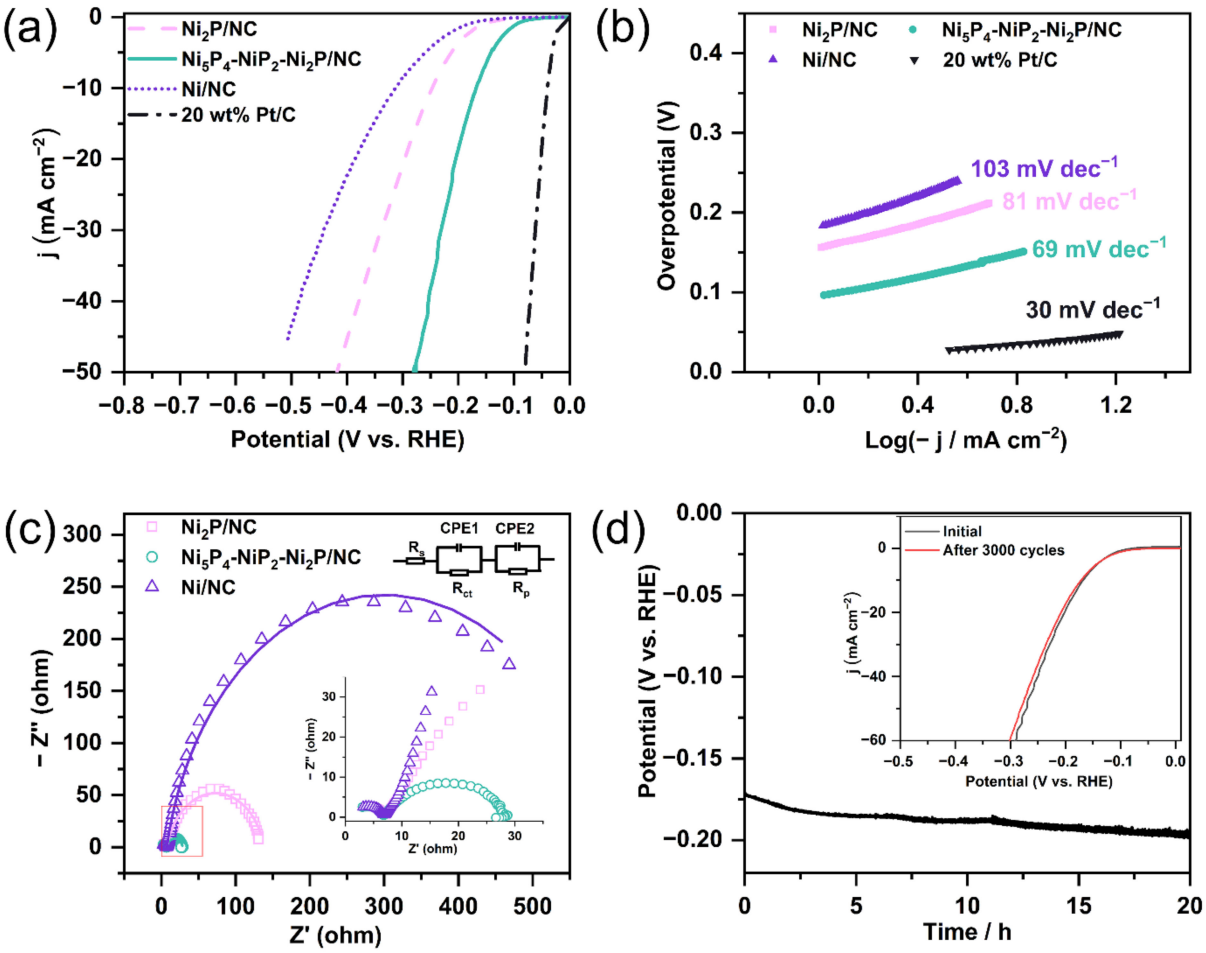

Figure 5. (**a**) Polarization curves of Ni/NC, Ni_2P/NC, Ni_5P_4-NiP_2-Ni_2P/NC, and Pt/C in the 0.5 M H_2SO_4; (**b**) the Tafel plots derived from Figure 5a; (**c**) Nyquist plots of Ni/NC, Ni_2P/NC, and Ni_5P_4-NiP_2-Ni_2P/NC at the overpotential of 170 mV; (**d**) Chronopotentiometric curves of the Ni_5P_4-NiP_2-Ni_2P/NC catalyst with a constant current density of 10 mA cm^{-2} for 70,000 s, insert is polarization curves of initial and after 3000 cycles of CV scans at 100 mV s^{-1}.

2.3. Electrochemical Performance in Alkaline Solution

The HER performances of Pt/C and three catalysts were also examined in 1 M KOH solution. In Figure 6a, the Ni_5P_4-NiP_2-Ni_2P/NC electrode achieves a catalytic current density of 10 mA cm^{-2} at an overpotential (η_{10}) of 202 mV, outperforming the electrodes Ni_2P/NC (234 mV) and Ni/NC (250 mV), suggesting an enhanced catalytic activity. The η_{10} of Ni_5P_4-NiP_2-Ni_2P/NC in alkaline solution is comparable to that of other nickel phosphide-based HER catalysts (Table S3). Similar to the test results in acidic solution, the Pt/C manifests the highest electrocatalytic activity and the fastest HER kinetics, with a Tafel slope of 48 mV dec^{-1}, cf. Figure 6b. The Tafel slopes of Ni_2P/NC, Ni_5P_4-NiP_2-Ni_2P/NC and Ni/NC are 80, 74, and 81 mV dec^{-1}, respectively, demonstrating that Ni_5P_4-NiP_2-Ni_2P/NC also possesses fast HER kinetics in alkaline solution. Moreover, the boosted HER kinetics of Ni_5P_4-NiP_2-Ni_2P/NC is further verified from its Nyquist plots, with a smaller semicircle diameter, as depicted in Figure 6c [55]. Additionally, Figure 6d shows the stability of the Ni_5P_4-NiP_2-Ni_2P/NC by chronopotentiometry and continuous CV scans. Although the potential at the current density of 10 mA cm^{-2} has a rapid negative shift of approximately 58 mV at first, it remains constant in the following 10 h. After accelerated degradation testing, the overpotential at 10 mA cm^{-2} increases by 50 mV. The XPS characterizations of Ni_5P_4-NiP_2-Ni_2P/NC after the 20 h chronopotentiometric experiment show that the intensity of the characteristic peaks of $Ni^{\delta+}$ (Ni $2p_{3/2}$: 853.1 and Ni $2p_{1/2}$: 870.8 eV, Figure S10) and $P^{\delta-}$ (P $2p_{3/2}$: 129.0 and P $2p_{1/2}$: 129.9 eV, Figure S11)

decreases obviously. The decrease in HER activity is attributed mainly to the decomposition of nickel phosphide species, owing to their exposure to air during the chronopotentiometry experiment. This result further indicates the nickel phosphide species plays a key role in electrocatalytic process towards HER.

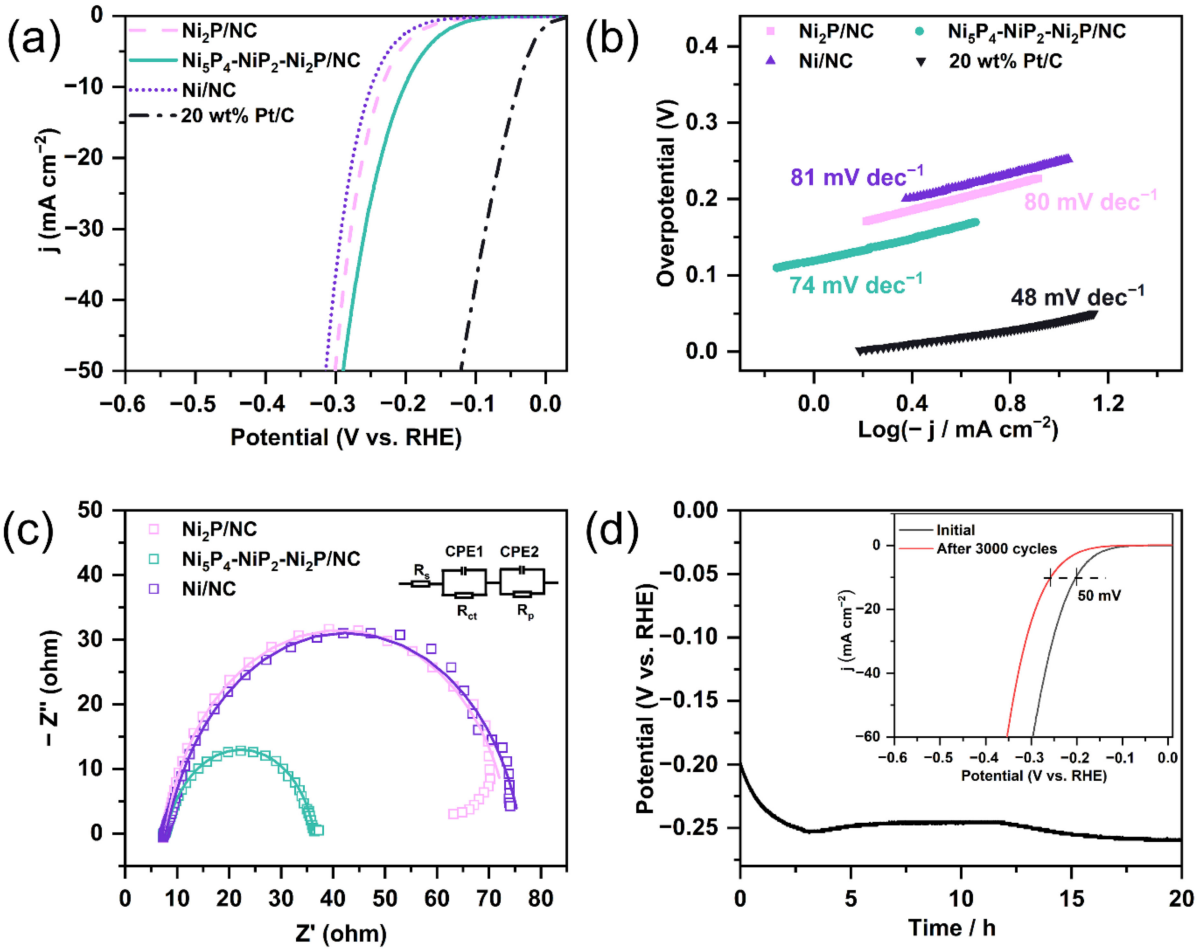

Figure 6. (**a**) Polarization curves of Ni/NC, Ni_2P/NC, Ni_5P_4-NiP_2-Ni_2P/NC, and Pt/C in the 1 M KOH; (**b**) the Tafel plots derived from Figure 6a; (**c**) Nyquist plots of Ni/NC, Ni_2P/NC, and Ni_5P_4-NiP_2-Ni_2P/NC at the overpotential of 220 mV; (**d**) Chronopotentiometric curves of Ni_5P_4-NiP_2-Ni_2P/NC catalyst with a constant current density of 10 mA cm^{-2} for 70,000 s in 1 M KOH, insert is polarization curves of initial and after 3000 cycles of CV scans at 100 mV s^{-1}.

2.4. Structure–Performance Analysis of Ni_5P_4-NiP_2-Ni_2P/NC

One can see that the catalyst Ni_5P_4-NiP_2-Ni_2P/NC exhibits enhanced catalytic activity related to Ni_2P/NC in both acidic and alkaline solutions. Generally, larger electrochemical active surface area (ECSA) value indicates exposure of more electro-active sites, which positively correlate with the HER activity. The C_{dl} values of the catalysts were tested in 0.5 M H_2SO_4 and 1 M KOH through measuring the non-Faradaic capacitive current using CV, cf. Figures S12 and S13. As observed from the fitting results, the ECSA follows the order of Ni_5P_4-NiP_2-Ni_2P/NC > Ni_2P/NC > Ni/NC in both acidic and alkaline solutions, cf. Figure 7a,b, and Table S4, which is in accordance with the activity trend. The polarization curves are normalized by the ECSA to compare the intrinsic HER activity of the catalysts. In Figure 7c,d, the Ni_5P_4-NiP_2-Ni_2P/NC catalyst still shows the highest HER activity among the three catalysts, with the smallest overpotential at the same current density, indicating its best intrinsic activity. These results demonstrate that the enhanced HER activity of Ni_5P_4-NiP_2-Ni_2P/NC arises from the enlarged ECSA and intrinsic activity that

could be endowed by the synergistic effect of Ni_5P_4-NiP_2-Ni_2P and the interconnected 3D mesoporous structure.

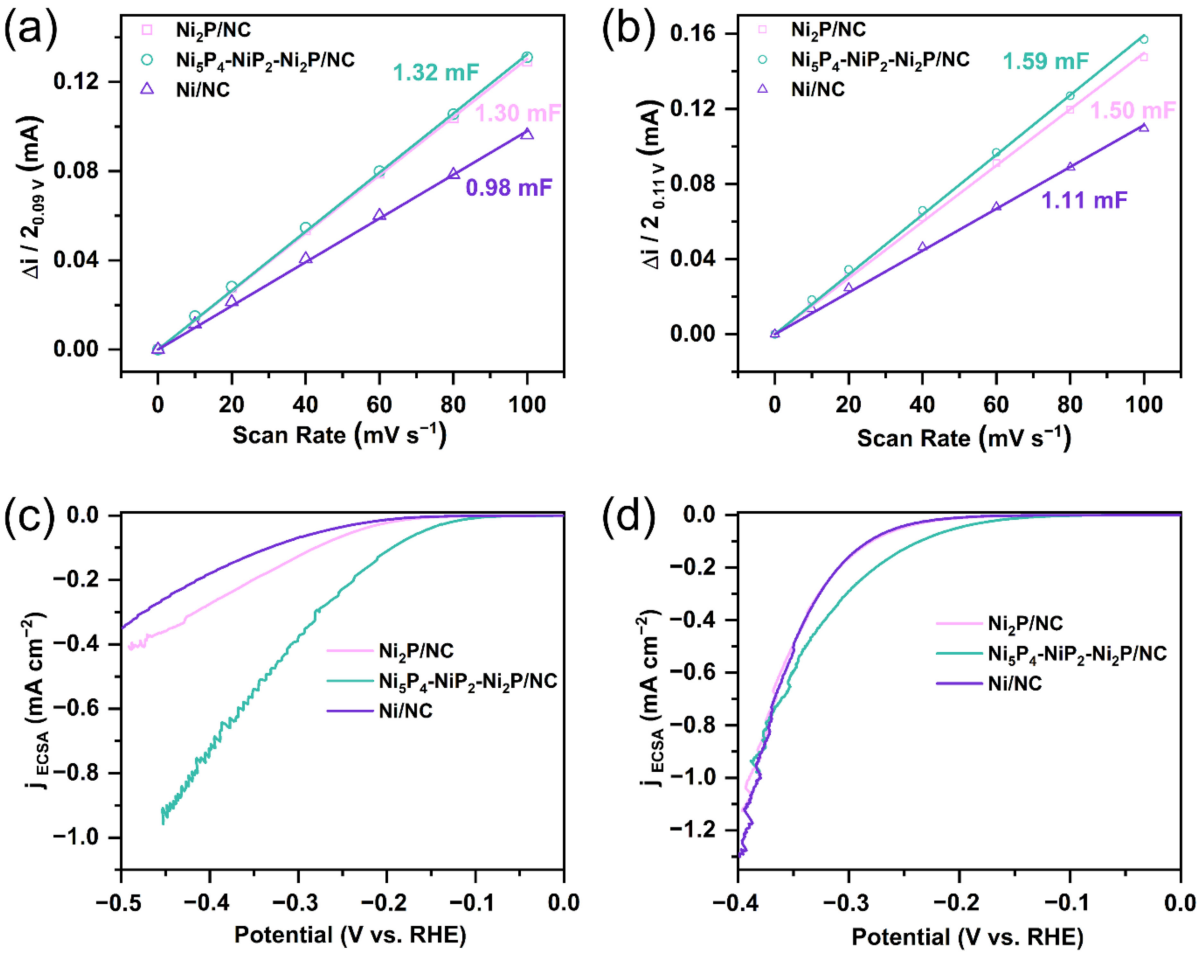

Figure 7. The capacitive currents of three samples were fitted as a function of scan rates from 10 mV s^{-1} to 100 mV s^{-1} in (**a**) 0.5 M H_2SO_4 and (**b**) 1 M KOH solutions; the polarization curves normalized by ECSA for the three catalysts in (**c**) 0.5 M H_2SO_4 and (**d**) 1 M KOH solutions.

3. Materials and Methods

3.1. Materials

All chemicals in this work were obtained from commercial sources and used without further purification. Urea (99%), nickel nitrate hexahydrate ($Ni(NO_3)_2{\cdot}6H_2O$, AR), 4,4′-bipyridine (bpy, 98%), dimethylglyoxime ($dmgH_2$, 98%), sodium borohydride ($NaBH_4$, 98%), sodium hypophosphite (NaH_2PO_2, 98%), and methanol (CH_3OH, AR) were purchased from Shanghai Titan Co., Ltd., Shanghai, China. Commercial Pt/C (20 wt% Pt, Hispec 3000) and Nafion solution (5% *w*/*w* in water and 1-propanol, D-520) were supplied by Alfa Aesar Chemicals Co. Ltd., Shanghai, China. Ultrapure water was purified by a Milli-Q system and used throughout this work.

3.2. Synthesis of $Ni(bpy)(NO_3)_2$/g-C_3N_4/$Ni(dmgH)_2$ Composites

Carbon nitride (g-C_3N_4) was prepared from urea following a reported method [56]. Typically, urea was placed in an alumina crucible with a cover and heated at 550 °C for 3 h in a muffle furnace. The resulting yellow powder (2.00 g) was dispersed to a mixed solution containing $Ni(NO_3)_2{\cdot}6H_2O$ (2.90 g), 4,4′-Bipyridine (bpy, 1.56 g), and CH_3OH (60 mL) through ultrasonication for 30 min. Then, the suspension was transferred to a 100 mL Teflon-lined autoclave and heated at 100 °C for 12 h. After being cooling to room temperature, the resultant hybrid $Ni(bpy)(NO_3)_2$/g-C_3N_4 was filtered, re-dispersed in 100 mL methanol,

and then treated with dimethylglyoxime ($dmgH_2$, 0.23 g) under vigorous stirring for 30 min. The product $Ni(bpy)(NO_3)_2/g\text{-}C_3N_4/Ni(dmgH)_2$ was collected via centrifugation, washed with CH_3OH for three times, and dried in a vacuum at 60 °C overnight.

3.3. Synthesis of Nitrogen-Doped Carbon-Twined Ni Nanoparticles

The hybrid precursor $Ni(bpy)(NO_3)_2/g\text{-}C_3N_4/Ni(dmgH)_2$ was pyrolyzed at 900 °C for 1 h under flowing N_2 atmosphere in a tube furnace. Before carbonization reaction, N_2 gas was passed through the furnace tube for 1 h to remove the air. The heating rate was 5 °C/min. The resultant product was labeled as Ni/NC.

3.4. Synthesis of Nitrogen-Doped Carbon/Carbon Nanotube Network Entangled with Nickel Phosphides Nanoparticles

Ni_5P_4-NiP_2-Ni_2P/NC was prepared by sodium borohydride ($NaBH_4$)-assisted phosphorization of Ni/NC. In detail, sodium hypophosphite (NaH_2PO_2, 2.00 g) and $NaBH_4$ (0.20 g) were mixed uniformly via grinding. Subsequently, the mixture of $NaBH_4/NaH_2PO_2$ and Ni/NC (0.20 g) was placed at the upstream and downstream of tube furnace, respectively. The furnace was heated to 600 °C for 1 h, with a heating rate of 5 °C/min under a N_2 atmosphere. After phosphorization, the black product was rinsed with distilled water and methanol and finally dried under vacuum at 60 °C, marked as Ni_5P_4-NiP_2-Ni_2P/NC. For comparison, the counterparts Ni_2P/NC and Ni/NC-B were prepared using the same procedure for Ni_5P_4-NiP_2-Ni_2P/NC but without $NaBH_4$ for the former and without NaH_2PO_2 for the latter.

3.5. Characterization Techniques

The crystalline phases were characterized by X-ray diffraction (XRD) analysis. Diffraction data were collected on a Rigaku Ultima IV diffractometer (Rigaku Co., Tokyo, Japan) with a scanning rate of 0.4°(2θ) min^{-1} using Cu-Kα (λ = 0.15406 nm) radiation at 40 kV and 30 mA. Scanning electron microscope (SEM) images were obtained using Phenom LE scanning electron microscope (Phenom-World, Eindhoven, Netherlands). High-resolution transmission electron microscope (HRTEM) images, selected area electron diffraction (SAED), and elemental mapping images were recorded on a FEI Tecnai G2 F20 microscope (FEI Co., Hillsboro, OR, USA) operated at an accelerating voltage of 200 kV, with a line resolution of 0.102 nm, a point resolution of 0.24 nm, and an information resolution of 0.14 nm. X-ray photoelectron spectroscopy (XPS) was measured on a Thermo Scientific K-Alpha X-ray photoelectron spectrometer (Thermo Scientific, Waltham, MA, USA) equipped with Al anode. Low-temperature nitrogen adsorption–desorption experiments were performed with a Quantachrome 3QDS-MP-30 instrument (Quantachrome Instruments, Boynton Beach, FL, USA). The specific surface area was calculated according to the Brunauer–Emmett–Teller (BET) method on the basis of the adsorption isotherm. The pore-size distribution was calculated using the density functional theory (DFT) method. Raman spectra were acquired on a Thermo DXR micro-Raman spectrometer (Thermo Scientific, Waltham, MA, USA) with a visible laser beam of 532 nm.

3.6. Electrochemical Test

Typically, 5.0 mg of the electrocatalyst was dispersed in 500 μL N,N-Dimethylformamide and 500 μL Nafion aqueous solutions (0.5%) by ultrasonication for 2 h to form the catalyst ink. Then, 8 μL of ink was dropped onto the polished glassy carbon disk of rotating disk electrode (RDE, diameter: 5 mm). The loading amount was 0.204 mg cm^{-2} for each catalyst on the electrode surface. The commercial 20 wt% Pt/C catalyst was also measured under the same conditions for comparison.

The electrochemical measurements were conducted in a standard three-electrode cell on a CHI760E electrochemical workstation. The glassy carbon RDE coated with the catalyst was used as the working electrode. The graphite rod and saturated calomel electrode (SCE)

were used as the counter and reference electrodes, respectively. All the potentials were reported with respect to the reversible hydrogen electrode (RHE) based on the equation:

$$E\ (V\ vs.\ RHE) = E\ (V\ vs.\ SCE) + 0.059\ pH + 0.24\ V \quad (1)$$

Linear sweep voltammetry (LSV) was recorded in Ar-saturated 0.5 M H_2SO_4 or 1 M KOH solution at a scan rate of 5 mV s^{-1}. The Tafel slope was calculated according to the equation:

$$\eta = b \log(-j/mA\ cm^{-2}) + a \quad (2)$$

where η, b, and j represent the overpotential ($\eta = 0\ V - E_{RHE}$), Tafel slope, and current density, respectively. The LSV polarization curves and corresponding Tafel plots were 95% internal resistance (iR)-corrected. Electrochemical impedance spectroscopy (EIS) measurements were performed with the frequency from 100 kHz to 0.1 Hz at the overpotentials of 170 mV and 220 mV in 0.5 M H_2SO_4 and 1 M KOH solutions, respectively. The EIS spectra were simulated using an equivalent circuit which consisted of a solution resistance (R_s) connected in series with two constant-phase element (CPE) that individually combined with the charge-transfer resistance (R_{ct}) and polarization resistance (R_p) in parallel. The electrochemical double-layer capacitance (C_{dl}) of each sample was measured between 0.04 and 0.14 V vs. RHE at the scan rate from 10 to 100 mV s^{-1}. The electrochemical active surface area (ECSA) was calculated on the basis of the equation:

$$ECSA = C_{dl}/C_s \quad (3)$$

where C_s is the specific capacitance, often assumed to be 40 μF·cm^{-2} [57]. The stability of Ni_5P_4-NiP_2-Ni_2P/NC was evaluated by accelerated degradation experiment and chronopotentiometry in both acidic and alkaline solutions. For accelerated degradation test, cyclic voltammetry (CV) measurement was performed with a scan rate of 100 mV s^{-1} between −0.32 V and 0.18 V vs. RHE for 3000 cycles, and the LSV curves before and after the cycling were recorded at 5 mV s^{-1}. Chronopotentiometry measurement was conducted under a constant current density of 10 mA cm^{-2} for up to 70,000 s.

4. Conclusions

In summary, we have reported an $NaBH_4$ assisted phosphorization strategy for the synthesis of ternary Ni_5P_4-NiP_2-Ni_2P nanocomposites dispersed in the N-doped carbon nanotubes and carbon particulates. The resultant product (Ni_5P_4-NiP_2-Ni_2P/NC) exhibits a better HER performance with a low overpotential and a small Tafel slope in 0.5 M H_2SO_4 and 1 M KOH electrolyte, related to the counterpart Ni_2P/NC. Furthermore, the Ni_5P_4-NiP_2-Ni_2P/NC catalyst holds a good stability in acidic solution. The enhancement of activity is attributed to the synergistic effect among three-component nickel phosphides and the support of 3D mesoporous carbon network. This work opens a new avenue to develop heterostructured electrocatalysts towards HER with high-performance.

Supplementary Materials: The following supporting information can be downloaded at: https://www.mdpi.com/article/10.3390/catal12121650/s1, Figure S1: (a) XRD pattern of the precursor $Ni(bpy)(NO_3)_2$/g-C_3N_4/$Ni(dmgH)_2$ and simulated XRD patterns of $Ni(bpy)(NO_3)_2$ and $Ni(dmgH)_2$, (b) and (c) the crystal structure of $Ni(bpy)(NO_3)_2$; Figure S2: X-ray photoelectron spectra of Ni/NC, Ni_2P/NC, Ni_5P_4-NiP_2-Ni_2P/NC, and Ni/NC-B; Figure S3: High-resolution XPS spectra of C 1s for the samples Ni/NC, Ni_2P/NC, and Ni_5P_4-NiP_2-Ni_2P/NC; Figure S4: High-resolution XPS spectrum of P 2s for the sample Ni_2P/NC; Figure S5: High-resolution XPS spectra of P 2s + B 1s for the sample Ni_5P_4-NiP_2-Ni_2P/NC; Figure S6: High-resolution XPS spectrum of B 1s for the sample Ni/NC-B; Figure S7: SEM image for Ni_5P_4-NiP_2-Ni_2P/NC after the chronopotentiometric test in 0.5 M H_2SO_4 solution; Figure S8: XPS high-resolution spectrum of Ni 2p for Ni_5P_4-NiP_2-Ni_2P/NC after the chronopotentiometric test in 0.5 M H_2SO_4 solution; Figure S9: XPS high-resolution spectrum of P 2p for Ni_5P_4-NiP_2-Ni_2P/NC after the chronopotentiometric test in 0.5 M H_2SO_4 solution; Figure S10: XPS high-resolution spectrum of Ni 2p for Ni_5P_4-NiP_2-Ni_2P/NC after the chronopotentiometric test

in 1 M KOH solution; Figure S11: XPS high-resolution spectrum of P 2p for Ni_5P_4-NiP_2-Ni_2P/NC after the chronopotentiometric test in 1 M KOH solution; Figure S12: Electrochemical double-layer capacitance (C_{dl}) measurements in 0.5 M H_2SO_4 for (a) Ni/NC, (b) Ni_2P/NC, and (c) Ni_5P_4-NiP_2-Ni_2P/NC using CV scans at different scan rates from 10 to 100 mV·s^{-1}; Figure S13: Electrochemical double-layer capacitance (C_{dl}) measurements in 1 M KOH for (a) Ni/NC, (b) Ni_2P/NC, and (c) Ni_5P_4-NiP_2-Ni_2P/NC using CV scans at different scan rates from 10 to 100 mV·s^{-1}; Table S1: Microstructural properties obtained by RRM for the sample Ni_5P_4-NiP_2-Ni_2P/NC; Table S2: Surface atomic compositions obtained from XPS spectra for the as-prepared samples; Table S3: Comparison of the HER Performance of the heterostructured catalysts comprising different nickel phosphides in the literatures and this work [3,15,25–30,32–35,37,38,52–54,58–61]; Table S4: Electrochemical active surface area (ECSA) of the as-prepared composites.

Author Contributions: M.P., methodology, validation, investigation, data curation, and writing—original draft preparation; X.S., methodology, resources, writing—review and editing, and funding acquisition; H.Z., investigation, funding acquisition, and writing—review and editing; L.A.E.-W., formal analysis, investigation; Y.G., data curation and investigation; T.J., J.H. and Y.W., methodology, validation, and data curation; J.Y. and Y.F., conceptualization, writing—original draft preparation, supervision, and funding acquisition. All authors have read and agreed to the published version of the manuscript.

Funding: This research was funded by the University Natural Science Research Project of Anhui Province (No. KJ2019A0549), Innovative Program of Anqing Normal University (202110732023 and XJ202110372019), Fundamental Research Funds for the Central Universities (ZY2117), the European Union (ERDF) 'Région Nouvelle Aquitaine', the Joint Funds of the National Natural Science Foundation of China (ZK20180055), Programs for Foreign Talent (G2021106012L) and the National Natural Science Foundation of China (22075290).

Data Availability Statement: Not applicable.

Acknowledgments: We are thankful for the help of the Analytical and Testing Centre of Anqing Research Institute, Beijing University of Chemical Technology, for the BET characterization.

Conflicts of Interest: The authors declare no conflict of interest.

References

1. Zhu, J.; Hu, L.; Zhao, P.; Lee, L.Y.S.; Wong, K.-Y. Recent Advances in Electrocatalytic Hydrogen Evolution Using Nanoparticles. *Chem. Rev.* **2020**, *120*, 851–918. [CrossRef] [PubMed]
2. Wang, H.-F.; Chen, L.; Pang, H.; Kaskel, S.; Xu, Q. MOF-Derived Electrocatalysts for Oxygen Reduction, Oxygen Evolution and Hydrogen Evolution Reactions. *Chem. Soc. Rev.* **2020**, *49*, 1414–1448. [CrossRef] [PubMed]
3. Zhang, H.; Li, W.; Feng, X.; Zhu, L.; Fang, Q.; Li, S.; Wang, L.; Li, Z.; Kou, Z. A Chainmail Effect of Ultrathin N-Doped Carbon Shell on Ni_2P Nanorod Arrays for Efficient Hydrogen Evolution Reaction Catalysis. *J. Colloid Interface Sci.* **2022**, *607*, 281–289. [CrossRef] [PubMed]
4. El-Refaei, S.M.; Russo, P.A.; Pinna, N. Recent Advances in Multimetal and Doped Transition-Metal Phosphides for the Hydrogen Evolution Reaction at Different pH values. *ACS Appl. Mater. Interfaces* **2021**, *13*, 22077–22097. [CrossRef] [PubMed]
5. Qin, Z.; Chen, Y.; Huang, Z.; Su, J.; Diao, Z.; Guo, L. Composition-Dependent Catalytic Activities of Noble-Metal-Free NiS/Ni_3S_4 for Hydrogen Evolution Reaction. *J. Phys. Chem. C* **2016**, *120*, 14581–14589. [CrossRef]
6. Li, Y.; Dai, T.; Wu, Q.; Lang, X.; Zhao, L.; Jiang, Q. Design Heterostructure of NiS-NiS_2 on NiFe Layered Double Hydroxide with Mo Doping for Efficient Overall Water Splitting. *Mater. Today Energy* **2022**, *23*, 100906. [CrossRef]
7. Wu, X.; Yang, B.; Li, Z.; Lei, L.; Zhang, X. Synthesis of Supported Vertical NiS_2 Nanosheets for Hydrogen Evolution Reaction in Acidic and Alkaline Solution. *RSC Adv.* **2015**, *5*, 32976–32982. [CrossRef]
8. Xing, Z.; Li, Q.; Wang, D.; Yang, X.; Sun, X. Self-Supported Nickel Nitride as an Efficient High-Performance Three-Dimensional Cathode for the Alkaline Hydrogen Evolution Reaction. *Electrochim. Acta* **2016**, *191*, 841–845. [CrossRef]
9. Yu, L.; Song, S.; McElhenny, B.; Ding, F.; Luo, D.; Yu, Y.; Chen, S.; Ren, Z. A Universal Synthesis Strategy to Make Metal Nitride Electrocatalysts for Hydrogen Evolution Reaction. *J. Mater. Chem. A* **2019**, *7*, 19728–19732. [CrossRef]
10. Zhai, L.; Benedict Lo, T.W.; Xu, Z.-L.; Potter, J.; Mo, J.; Guo, X.; Tang, C.C.; Edman Tsang, S.C.; Lau, S.P. In Situ Phase Transformation on Nickel-Based Selenides for Enhanced Hydrogen Evolution Reaction in Alkaline Medium. *ACS Energy Lett.* **2020**, *5*, 2483–2491. [CrossRef]
11. Liu, P.; Rodriguez, J.A. Catalysts for Hydrogen Evolution from the [NiFe] Hydrogenase to the Ni_2P(001) Surface: The Importance of Ensemble Effect. *J. Am. Chem. Soc.* **2005**, *127*, 14871–14878. [CrossRef]
12. Brazzolotto, D.; Gennari, M.; Queyriaux, N.; Simmons, T.R.; Pécaut, J.; Demeshko, S.; Meyer, F.; Orio, M.; Artero, V.; Duboc, C. Nickel-Centred Proton Reduction Catalysis in a Model of [NiFe] Hydrogenase. *Nat. Chem.* **2016**, *8*, 1054–1060. [CrossRef]

13. Moon, J.-S.; Jang, J.-H.; Kim, E.-G.; Chung, Y.-H.; Yoo, S.J.; Lee, Y.-K. The Nature of Active Sites of Ni_2P Electrocatalyst for Hydrogen Evolution Reaction. *J. Catal.* **2015**, *326*, 92–99. [CrossRef]
14. Feng, L.; Vrubel, H.; Bensimon, M.; Hu, X. Easily-Prepared Dinickel Phosphide (Ni_2P) Nanoparticles as an Efficient and Robust Electrocatalyst for Hydrogen Evolution. *Phys. Chem. Chem. Phys.* **2014**, *16*, 5917–5921. [CrossRef]
15. He, S.; He, S.; Bo, X.; Wang, Q.; Zhan, F.; Wang, Q.; Zhao, C. Porous Ni_2P/C Microrods Derived from Microwave-Prepared MOF-74-Ni and Its Electrocatalysis for Hydrogen Evolution Reaction. *Mater. Lett.* **2018**, *231*, 94–97. [CrossRef]
16. Yan, L.; Dai, P.; Wang, Y.; Gu, X.; Li, L.; Cao, L.; Zhao, X. In Situ Synthesis Strategy for Hierarchically Porous Ni_2P Polyhedrons from MOFs Templates with Enhanced Electrochemical Properties for Hydrogen Evolution. *ACS Appl. Mater. Interfaces* **2017**, *9*, 11642–11650. [CrossRef]
17. Bai, Y.; Zhang, H.; Li, X.; Liu, L.; Xu, H.; Qiu, H.; Wang, Y. Novel Peapod-like Ni_2P Nanoparticles with Improved Electrochemical Properties for Hydrogen Evolution and Lithium Storage. *Nanoscale* **2015**, *7*, 1446–1453. [CrossRef]
18. Sun, H.; Xu, X.; Yan, Z.; Chen, X.; Cheng, F.; Weiss, P.S.; Chen, J. Porous Multishelled Ni_2P Hollow Microspheres as an Active Electrocatalyst for Hydrogen and Oxygen Evolution. *Chem. Mater.* **2017**, *29*, 8539–8547. [CrossRef]
19. Liu, C.; Gong, T.; Zhang, J.; Zheng, X.; Mao, J.; Liu, H.; Li, Y.; Hao, Q. Engineering Ni_2P-$NiSe_2$ Heterostructure Interface for Highly Efficient Alkaline Hydrogen Evolution. *Appl. Catal. B Environ.* **2020**, *262*, 118245. [CrossRef]
20. Nguyen, C.D.; Nguyen, V.-H.; Pham, L.M.T.; Vu, T.Y. Three-Dimensional Ni_2P-MoP_2 Mesoporous Nanorods Array as Self-Standing Electrocatalyst for Highly Efficient Hydrogen Evolution. *Int. J. Hydrogen Energy* **2020**, *45*, 15063–15075. [CrossRef]
21. Jin, M.; Zhang, X.; Shi, R.; Lian, Q.; Niu, S.; Peng, O.; Wang, Q.; Cheng, C. Hierarchical CoP@Ni_2P Catalysts for pH-Universal Hydrogen Evolution at High Current Density. *Appl. Catal. B Environ.* **2021**, *296*, 120350. [CrossRef]
22. Xiao, X.; Huang, D.; Fu, Y.; Wen, M.; Jiang, X.; Lv, X.; Li, M.; Gao, L.; Liu, S.; Wang, M.; et al. Engineering NiS/Ni_2P Heterostructures for Efficient Electrocatalytic Water Splitting. *ACS Appl. Mater. Interfaces* **2018**, *10*, 4689–4696. [CrossRef] [PubMed]
23. Zeng, L.; Sun, K.; Wang, X.; Liu, Y.; Pan, Y.; Liu, Z.; Cao, D.; Song, Y.; Liu, S.; Liu, C. Three-Dimensional-Networked Ni_2P/Ni_3S_2 Heteronanoflake Arrays for Highly Enhanced Electrochemical Overall-Water-Splitting Activity. *Nano Energy* **2018**, *51*, 26–36. [CrossRef]
24. Wu, L.; Yu, L.; Zhang, F.; McElhenny, B.; Luo, D.; Karim, A.; Chen, S.; Ren, Z. Heterogeneous Bimetallic Phosphide Ni_2P-Fe_2P as an Efficient Bifunctional Catalyst for Water/Seawater Splitting. *Adv. Funct. Mater.* **2021**, *31*, 2006484. [CrossRef]
25. Liu, T.; Li, A.; Wang, C.; Zhou, W.; Liu, S.; Guo, L. Interfacial Electron Transfer of Ni_2P-NiP_2 Polymorphs Inducing Enhanced Electrochemical Properties. *Adv. Mater.* **2018**, *30*, 1803590. [CrossRef]
26. Hong, W.; Lv, C.; Sun, S.; Chen, G. Fabrication and Study of the Synergistic Effect of Janus Ni_2P/Ni_5P_4 Embedded in N-Doped Carbon as Efficient Electrocatalysts for Hydrogen Evolution Reaction. *Catal. Sci. Technol.* **2020**, *10*, 1023–1029. [CrossRef]
27. Ding, G.; Zhang, Y.; Dong, J.; Xu, L. Fabrication of Ni_2P/Ni_5P_4 Nanoparticles Embedded in Three-Dimensional N-Doped Graphene for Acidic Hydrogen Evolution Reaction. *Mater. Lett.* **2021**, *299*, 130071. [CrossRef]
28. Wang, X.; Kolen'ko, Y.V.; Bao, X.-Q.; Kovnir, K.; Liu, L. One-Step Synthesis of Self-Supported Nickel Phosphide Nanosheet Array Cathodes for Efficient Electrocatalytic Hydrogen Generation. *Angew. Chem. Int. Ed.* **2015**, *54*, 8188–8192. [CrossRef]
29. Wang, Z.; Wang, S.; Ma, L.; Guo, Y.; Sun, J.; Zhang, N.; Jiang, R. Water-Induced Formation of Ni_2P-$Ni_{12}P_5$ Interfaces with Superior Electrocatalytic Activity toward Hydrogen Evolution Reaction. *Small* **2021**, *17*, 2006770. [CrossRef]
30. Shi, H.; Yu, Q.; Liu, G.; Hu, X. Promoted Electrocatalytic Hydrogen Evolution Performance by Constructing $Ni_{12}P_5$-Ni_2P Heterointerfaces. *Int. J. Hydrogen Energy* **2021**, *46*, 17097–17105. [CrossRef]
31. Liu, J.; Zhu, D.; Zheng, Y.; Vasileff, A.; Qiao, S.-Z. Self-Supported Earth-Abundant Nanoarrays as Efficient and Robust Electrocatalysts for Energy-Related Reactions. *ACS Catal.* **2018**, *8*, 6707–6732. [CrossRef]
32. Cai, W.; Liu, W.; Sun, H.; Li, J.; Yang, L.; Liu, M.; Zhao, S.; Wang, A. Ni_5P_4-NiP_2 Nanosheet Matrix Enhances Electron-Transfer Kinetics for Hydrogen Recovery in Microbial Electrolysis Cells. *Appl. Energy* **2018**, *209*, 56–64. [CrossRef]
33. Zhang, J.; Zhang, Z.; Ji, Y.; Yang, J.; Fan, K.; Ma, X.; Wang, C.; Shu, R.; Chen, Y. Surface Engineering Induced Hierarchical Porous $Ni_{12}P_5$-Ni_2P Polymorphs Catalyst for Efficient Wide pH Hydrogen Production. *Appl. Catal. B Environ.* **2021**, *282*, 119609. [CrossRef]
34. Yan, Y.; Lin, J.; Bao, K.; Xu, T.; Qi, J.; Cao, J.; Zhong, Z.; Fei, W.; Feng, J. Free-Standing Porous Ni_2P-Ni_5P_4 Heterostructured Arrays for Efficient Electrocatalytic Water Splitting. *J. Colloid Interface Sci.* **2019**, *552*, 332–336. [CrossRef]
35. Pan, Y.; Hu, W.; Liu, D.; Liu, Y.; Liu, C. Carbon Nanotubes Decorated with Nickel Phosphide Nanoparticles as Efficient Nanohybrid Electrocatalysts for the Hydrogen Evolution Reaction. *J. Mater. Chem. A* **2015**, *3*, 13087–13094. [CrossRef]
36. Cong, Y.; Huang, S.; Mei, Y.; Li, T.-T. Metal-Organic Frameworks-Derived Self-Supported Carbon-Based Composites for Electrocatalytic Water Splitting. *Chem. Eur. J.* **2021**, *27*, 15866–15888. [CrossRef]
37. Miao, M.; Hou, R.; Liang, Z.; Qi, R.; He, T.; Yan, Y.; Qi, K.; Liu, H.; Feng, G.; Xia, B.Y. Chainmail Catalyst of Ultrathin P-Doped Carbon Shell-Encapsulated Nickel Phosphides on Graphene towards Robust and Efficient Hydrogen Generation. *J. Mater. Chem. A* **2018**, *6*, 24107–24113. [CrossRef]
38. Chen, L.; Wu, P.; Yang, S.; Qian, K.; Sun, W.; Wei, W.; Xu, Y.; Xie, J. Fabrication of CNTs Encapsulated Nickel-Nickel Phosphide Nanoparticles on Graphene for Remarkable Hydrogen Evolution Reaction Performance. *J. Electroanal. Chem.* **2019**, *846*, 113142. [CrossRef]

39. Lan, W.; Li, D.; Wang, W.; Liu, Z.; Chen, H.; Xu, Y. Multi-Walled Carbon Nanotubes Reinforced Nickel Phosphide Composite: As an Efficient Electrocatalyst for Hydrogen Evolution Reaction by One-Step Powder Sintering. *Int. J. Hydrogen Energy* **2020**, *45*, 412–423. [CrossRef]
40. Ren, J.-T.; Chen, L.; Wang, Y.-S.; Tian, W.-W.; Gao, L.-J.; Yuan, Z.-Y. FeNi Nanoalloys Encapsulated in N-Doped CNTs Tangled with N-Doped Carbon Nanosheets as Efficient Multifunctional Catalysts for Overall Water Splitting and Rechargeable Zn-Air Batteries. *ACS Sustain. Chem. Eng.* **2020**, *8*, 223–237. [CrossRef]
41. Mehtab, A.; Alshehri, S.M.; Ahmad, T. Photocatalytic and Photoelectrocatalytic Water Splitting by Porous g-C_3N_4 Nanosheets for Hydrogen Generation. *ACS Appl. Nano Mater.* **2022**, *5*, 12656–12665. [CrossRef]
42. Cao, S.-W.; Yuan, Y.-P.; Barber, J.; Loo, S.C.J.; Xue, C. Noble-Metal-Free g-C_3N_4/Ni(dmgH)$_2$ Composite for Efficient Photocatalytic Hydrogen Evolution under Visible Light Irradiation. *Appl. Surf. Sci.* **2014**, *319*, 344–349. [CrossRef]
43. Yan, X.; Gu, M.; Wang, Y.; Xu, L.; Tang, Y.; Wu, R. In-Situ Growth of Ni Nanoparticle-Encapsulated N-Doped Carbon Nanotubes on Carbon Nanorods for Efficient Hydrogen Evolution Electrocatalysis. *Nano Res.* **2020**, *13*, 975–982. [CrossRef]
44. Zhong, H.; Estudillo-Wong, L.A.; Gao, Y.; Feng, Y.; Alonso-Vante, N. Cobalt-Based Multicomponent Oxygen Reduction Reaction Electrocatalysts Generated by Melamine Thermal Pyrolysis with High Performance in an Alkaline Hydrogen/Oxygen Microfuel Cell. *ACS Appl. Mater. Interfaces* **2020**, *12*, 21605–21615. [CrossRef]
45. Chang, J.; Zang, S.; Li, J.; Wu, D.; Lian, Z.; Xu, F.; Jiang, K.; Gao, Z. Nitrogen-Doped Porous Carbon Encapsulated Nickel Iron Alloy Nanoparticles, One-Step Conversion Synthesis for Application as Bifunctional Catalyst for Water Electrolysis. *Electrochim. Acta* **2021**, *389*, 138785. [CrossRef]
46. Farooq, U.; Ahmed, J.; Alshehri, S.M.; Ahmad, T. High-Surface-Area Sodium Tantalate Nanoparticles with Enhanced Photocatalytic and Electrical Properties Prepared through Polymeric Citrate Precursor Route. *ACS Omega* **2019**, *4*, 19408–19419. [CrossRef]
47. Farooq, U.; Phul, R.; Alshehri, S.M.; Ahmed, J.; Ahmad, T. Electrocatalytic and Enhanced Photocatalytic Applications of Sodium Niobate Nanoparticles Developed by Citrate Precursor Route. *Sci. Rep.* **2019**, *9*, 4488. [CrossRef]
48. Farooq, U.; Ahmed, J.; Alshehri, S.M.; Mao, Y.; Ahmad, T. Self-Assembled Interwoven Nanohierarchitectures of $NaNbO_3$ and $NaNb_{1-x}Ta_xO_3$ ($0.05 \leq x \leq 0.20$): Synthesis, Structural Characterization, Photocatalytic Applications, and Dielectric Properties. *ACS Omega* **2022**, *7*, 16952–16967. [CrossRef]
49. Kondo, T.; Casolo, S.; Suzuki, T.; Shikano, T.; Sakurai, M.; Harada, Y.; Saito, M.; Oshima, M.; Trioni, M.I.; Tantardini, G.F.; et al. Atomic-Scale Characterization of Nitrogen-Doped Graphite: Effects of Dopant Nitrogen on the Local Electronic Structure of the Surrounding Carbon Atoms. *Phys. Rev. B* **2012**, *86*, 035436. [CrossRef]
50. Xu, H.; Jia, H.; Fei, B.; Ha, Y.; Li, H.; Guo, Y.; Liu, M.; Wu, R. Charge Transfer Engineering via Multiple Heteroatom Doping in Dual Carbon-Coupled Cobalt Phosphides for Highly Efficient Overall Water Splitting. *Appl. Catal. B Environ.* **2020**, *268*, 118404. [CrossRef]
51. Zhou, G.; Ma, Y.; Wu, X.; Lin, Y.; Pang, H.; Zhang, M.; Xu, L.; Tian, Z.; Tang, Y. Electronic Modulation by N Incorporation Boosts the Electrocatalytic Performance of Urchin-Like Ni_5P_4 Hollow Microspheres for Hydrogen Evolution. *Chem. Eng. J.* **2020**, *402*, 126302. [CrossRef]
52. Li, Y.; Cai, P.; Ci, S.; Wen, Z. Strongly Coupled 3D Nanohybrids with Ni_2P/Carbon Nanosheets as pH-Universal Hydrogen Evolution Reaction Electrocatalysts. *ChemElectroChem* **2017**, *4*, 340–344. [CrossRef]
53. He, S.; He, S.; Gao, F.; Bo, X.; Wang, Q.; Chen, X.; Duan, J.; Zhao, C. Ni_2P@Carbon Core-Shell Nanorod Array Derived from ZIF-67-Ni: Effect of Phosphorization Temperature on Morphology, Structure and Hydrogen Evolution Reaction Performance. *Appl. Surf. Sci.* **2018**, *457*, 933–941. [CrossRef]
54. Tian, T.; Ai, L.; Jiang, J. Metal-Organic Framework-Derived Nickel Phosphides as Efficient Electrocatalysts toward Sustainable Hydrogen Generation from Water Splitting. *RSC Adv.* **2015**, *5*, 10290–10295. [CrossRef]
55. Dai, J.; Zhu, Y.; Tahini, H.A.; Lin, Q.; Chen, Y.; Guan, D.; Zhou, C.; Hu, Z.; Lin, H.-J.; Chan, T.-S.; et al. Single-Phase Perovskite Oxide with Super-Exchange Induced Atomic-Scale Synergistic Active Centers Enables Ultrafast Hydrogen Evolution. *Nat. Commun.* **2020**, *11*, 5657. [CrossRef]
56. Zhang, Y.; Liu, J.; Wu, G.; Chen, W. Porous Graphitic Carbon Nitride Synthesized via Direct Polymerization of Urea for Efficient Sunlight-Driven Photocatalytic Hydrogen Production. *Nanoscale* **2012**, *4*, 5300–5303. [CrossRef]
57. Ji, X.; Wang, K.; Zhang, Y.; Sun, H.; Zhang, Y.; Ma, T.; Ma, Z.; Hu, P.; Qiu, Y. MoC Based Mott-Schottky Electrocatalyst for Boosting the Hydrogen Evolution Reaction Performance. *Sustain. Energy Fuels* **2020**, *4*, 407–416. [CrossRef]
58. Wang, X.; Kolen'ko, Y.V.; Liu, L. Direct Solvothermal Phosphorization of Nickel Foam to Fabricate Integrated Ni_2P-Nanorods/Ni Electrodes for Efficient Electrocatalytic Hydrogen Evolution. *Chem. Commun.* **2015**, *51*, 6738–6741. [CrossRef]
59. Huo, S.; Yang, S.; Niu, Q.; Yang, F.; Song, L. Synthesis of Functional Ni_2P/CC Catalyst and the Robust Performances in Hydrogen Evolution Reaction and Nitrate Reduction. *Int. J. Hydrogen Energy* **2020**, *45*, 4015–4025. [CrossRef]
60. Fu, Q.; Wang, X.; Han, J.; Zhong, J.; Zhang, T.; Yao, T.; Xu, C.; Gao, T.; Xi, S.; Liang, C.; et al. Phase-Junction Electrocatalysts towards Enhanced Hydrogen Evolution Reaction in Alkaline Media. *Angew. Chem. Int. Ed.* **2021**, *60*, 259–267. [CrossRef]
61. Chen, A.; Fu, L.; Xiang, W.; Wei, W.; Liu, D.; Liu, C. Facile Synthesis of Ni_5P_4 Nanosheets/Nanoparticles for Highly Active and Durable Hydrogen Evolution. *Int. J. Hydrogen Energy* **2021**, *46*, 11701–11710. [CrossRef]